INTERNATIONAL JOURNAL FOR NUMERICAL METHODS IN FLUIDS
*Int. J. Numer. Meth. Fluids* 2007; **54**:1239–1268
Published online 21 February 2007 in Wiley InterScience (www.interscience.wiley.com). DOI: 10.1002/fld.1439

# Resolution of the Navier–Stokes equations on block-structured meshes

C. Romé, S. Glockner*, † and J. P. Caltagirone

*Laboratoire TREFLE, CNRS-UMR 8508, 16 av. Pey-Berland, 33607 PESSAC Cedex, France*

SUMMARY

We propose a non-iterative method to connect non-matching block-structured meshes applied to the resolution of the Navier–Stokes equations. The present article gives a complete description of the method based on the implicit treatment of the connecting condition. We also extend it to curvilinear meshes. The spatial convergence order of the method is shown to be two and the approach is validated on different 2D laminar flows frequently found in the literature. Copyright © 2007 John Wiley & Sons, Ltd.

Received 12 September 2006; Revised 1 December 2006; Accepted 6 December 2006

KEY WORDS: block-structured meshes; Navier–Stokes; non-matching; non-conforming; overlapping; interpolation

## 1. INTRODUCTION

A key step in a numerical simulation is the generation of a mesh, the first function of which is to accurately follow the contour lines of the geometry. Generally speaking, meshes can be distinguished as structured or unstructured, Cartesian or curvilinear, orthogonal or not, monoblock or multiblock, etc. The starting point of this work is a computational fluid dynamics (CFD) code written for one curvilinear, structured and orthogonal block. To extend its use to complex geometries, it was natural to work on block-structured meshes. The freedom given by non-matching interfaces allows geometry curves to be followed more precisely thanks to the fact that the blocks are independent.

We first present the numerical context of this work by describing the models and numerical methods of our CFD code Aquilon (Aq. on the figures and tables) and continue with a presentation of the domain decomposition framework.

Next, we propose a method, first introduced in [1], of connecting non-conforming meshes. It is non-iterative and relies on the implicit treatment of the interface condition. We apply it to

*Correspondence to: S. Glockner, Laboratoire TREFLE, CNRS-UMR 8508, 16 av. Pey-Berland, 33607 PESSAC Cedex, France.
†E-mail: glockner@enscpb.fr

the Navier–Stokes equations for laminar divergence-free flows in the framework of the augmented Lagrangian method. Special attention is paid to the interpolation techniques used. For a better comprehension of the implementation of the method, we present it first for Cartesian block-structured meshes and then generalize to orthogonal curvilinear coordinate systems.

Finally, we show that the spatial convergence order of the method is two and validate it on academic test cases such as the flow over a backward facing step, the lid-driven cavity flow and the flow around a cylinder (stationary or not).

## 2. NUMERICAL CONTEXT

### *2.1. Numerical methods*

We are interested in the incompressible Navier–Stokes equations:

$$\nabla \cdot \mathbf{u} = 0 \tag{1}$$

$$\rho \left( \frac{\partial \mathbf{u}}{\partial t} + \nabla \cdot (\mathbf{u} \otimes \mathbf{u}) \right) = -\nabla p + \nabla \cdot \mu(\nabla \mathbf{u} + \nabla^{\mathrm{t}} \mathbf{u}) \tag{2}$$

The implementation of the boundary conditions is done thanks to a penalization technique which derives from a Fourier boundary condition found in thermal science [2] and expressed by

$$\frac{\partial T}{\partial n} + Bi(T - T_\infty) = 0 \tag{3}$$

where $T$ is the temperature, $T_\infty$ a reference temperature, and $Bi$ the Biot number. According to the values of $Bi$, one can impose a Dirichlet condition ($Bi = \infty$), a Neumann condition ($Bi = 0$), or a Fourier condition if the value of $Bi$ is bounded between 0 and $\infty$.

A penalization term is added to the Navier–Stokes equations, written $\mathbf{BIU}(\mathbf{u} - \mathbf{u}_\infty)$ where $\mathbf{BIU}$ is an order 2 diagonal tensor of component ($BIU_u$, $BIU_v$), with $0 \leqslant BIU_u \leqslant \infty$ and $0 \leqslant BIU_v \leqslant \infty$.

Thus, the Navier–Stokes system can be written as

$$\begin{gathered} \nabla \cdot \mathbf{u} = 0 \quad \text{on } \Omega \\ \rho \left( \frac{\partial \mathbf{u}}{\partial t} + \nabla \cdot (\mathbf{u} \otimes \mathbf{u}) \right) + \mathbf{BIU}(\mathbf{u} - \mathbf{u}_\infty) = -\nabla p + \nabla \cdot \mu(\nabla \mathbf{u} + \nabla^{\mathrm{t}} \mathbf{u}) \quad \text{on } \Omega \\ (\nabla \mathbf{u}) \cdot \mathbf{n} = 0 \quad \text{on } \partial\Omega \end{gathered} \tag{4}$$

Time implicit discretization is used and the inertial term is linearized at order one. The resolution of the Navier–Stokes equations requires a consistent pressure and a divergence-free velocity field to be obtained at each time step. This coupling is difficult to treat for incompressible flows where pressure does not appear explicitly in the mass conservation equations. Two classes of methods exist, depending on the fact whether the Navier–Stokes operator is split or not:

- None time splitting and exact space methods:
  - Coupled resolution of velocity and pressure. It is tedious and complex because the matrices are very ill conditioned.
  - Artificial compressibility method described by Peyret and Taylor [3]. It takes into account a perturbation parameter which acts on pressure in the mass continuity equation. Pressure



DOI: 10.1002/fld

is eliminated from the momentum equations. This technique often gives ill-conditioned matrices and needs an iterative method such as the Uzawa algorithm [4].
  - Implicit approaches which are minimization methods under constraint. The augmented Lagrangian method is one of them and has been analysed by Fortin and Glowinski [5]. It is used in our code for laminar, incompressible, turbulent, multiphase flows [2, 6–9] and is described later on.

- Time splitting methods. These consist of a prediction/diffusion step and a correction/projection one for the velocity and pressure field. The following methods are often distinguished:
  - Projection methods introduced by Chorin [10, 11] and their variants [12, 13].
  - Incremental methods for the pressure correction introduced by Goda [14] and then improved by Timmermans *et al*. [15].
  - Prediction/correction algorithms such as SIMPLE (semi implicit method for pressure linked equations) or SIMPLER (SIMPLE revised) [16, 17] which use a pressure correction equation to modify the velocity field.

*2.1.1. The augmented Lagrangian method.* The book of Fortin and Glowinsky [5] presents numerous applications of this method applied to the resolution of partial differential equations, especially the Stokes and Navier–Stokes problems. The Stokes system is formulated as a velocity–pressure minimization–maximization problem requiring the computation of a saddle point ($\mathbf{u}$, $p$) associated with the augmented Lagrangian of the problem. The pressure is considered as a Lagrange multiplier and the incompressibility constraint is introduced implicitly into the momentum equations. Then, the saddle-point ($\mathbf{u}$, $p$) is computed using an iterative Uzawa algorithm. On a more formal point of view, if

$$L^2(\Omega) = \left\{ f, \int_\Omega |f|^2 \, \mathrm{d}\Omega < \infty \right\}$$

$$H_0^1(\Omega) = \left\{ f \in L^2(\Omega), \frac{\partial f}{\partial x_i} \in L^2(\Omega), \ i \in [1,3], \ f|_{\partial\Omega} = 0 \right\}$$

a functional $J(\mathbf{v})$ is defined for each $\mathbf{v} \in H_0^1(\Omega)$, resulting from the weak formulation of the momentum equations, and has to be minimized under the constraint

$$M = \{\mathbf{v} \in H_0^1(\Omega), \ \nabla \cdot \mathbf{v} = 0\}$$

which is equivalent to find $\mathbf{u} \in M$ such as

$$J(\mathbf{u}) = \min_{\mathbf{v} \in M}(J(\mathbf{v})) \tag{5}$$

The constraint is then satisfied thanks to a Lagrange multiplier $q$, transforming the problem with the constraint $M$ to a problem without constraint. The Lagrangian is defined as

$$\begin{aligned} &L : M \times L^2 \to \Re \\ &(\mathbf{v}, q) \mapsto L_r(\mathbf{v}, q) = J(\mathbf{v}) - \int_\Omega q \nabla \cdot \mathbf{v} \, \mathrm{d}\Omega \end{aligned} \tag{6}$$



DOI: 10.1002/fld

The minimization problem consists of finding the saddle-point $(\mathbf{u}, p) \in M \times L^2$ of the Lagrangian $L$ which verifies

$$\begin{aligned} L(\mathbf{u}, p) &= \min_{\mathbf{v}\in M}\left(\max_{q\in L^2}(L(\mathbf{v}, q))\right) \\ &= \max_{q\in L^2}\left(\min_{\mathbf{v}\in M}(L(\mathbf{v}, q))\right) \end{aligned} \tag{7}$$

To improve the convergence properties, for each $(\mathbf{v}, q) \in M \times L^2$, the augmented Lagrangian is defined as

$$\begin{aligned} &L_r : M \times L^2 \to \Re \\ &(\mathbf{v}, q) \mapsto L_r(\mathbf{v}, q) = J(\mathbf{v}) - \int_\Omega q\nabla\cdot\mathbf{v}\,\mathrm{d}\Omega + \int_\Omega \frac{\mathrm{d}r}{2}|\nabla\cdot\mathbf{v}|^2\,\mathrm{d}\Omega \end{aligned} \tag{8}$$

A saddle-point of $L$ is also a saddle-point of $L_r$ (and reciprocally). It is demonstrated for the Stokes problem and admitted for the Navier–Stokes equations, that, coming back to the strong formulation, the saddle-point is also the solution of the system

$$\begin{gathered} \nabla\cdot\mathbf{u} = 0 \\ \rho\left(\frac{\partial\mathbf{u}}{\partial t} + \nabla\cdot(\mathbf{u}\otimes\mathbf{u})\right) + \mathbf{BIU}(\mathbf{u}-\mathbf{u}_\infty) = -\nabla p + \nabla\cdot\mu(\nabla\mathbf{u} + \nabla^{\mathrm{t}}\mathbf{u}) - \mathrm{d}r\nabla(\nabla\cdot\mathbf{u}) \end{gathered} \tag{9}$$

The calculation of the solution is done thanks to the Uzawa iterative method [5] which generates the following $k$-iterations $(\mathbf{u}^k, p^k)$ that can be stopped by setting a criterion based on the divergence of the velocity field, i.e. $\|\nabla\cdot\mathbf{u}\| \leqslant \varepsilon$, with $\varepsilon$ small

**Initialization**
$\mathbf{u}^{k=0} = \mathbf{u}^n$ and $p^{k=0} = p^n$
**Iterations**
*for* $k = 0, K-1$
*computation of* $\mathbf{u}^{k+1}$ *solution of*:

$$\begin{aligned} &\rho^n\left(\frac{\mathbf{u}^{k+1}}{\Delta t} + \nabla\cdot(\mathbf{u}^{k+1}\otimes\mathbf{u}^k) - \mathbf{u}^{k+1}\nabla\cdot\mathbf{u}^k\right) + \mathbf{BIU}(\mathbf{u}^{k+1} - \mathbf{u}_\infty) \\ &\quad = -\nabla p^k + \nabla\cdot\mu(\nabla\mathbf{u}^{k+1} + \nabla^t\mathbf{u}^{k+1}) + dr\nabla(\nabla\cdot\mathbf{u}^{k+1}) + \rho\frac{\mathbf{u}^k}{\Delta t} \end{aligned} \tag{10}$$

*updating of* $p^{k+1}$ *with*:
$p^{k+1} = p^k - dp\nabla\cdot\mathbf{u}^{k+1}$
**Solution**
$\mathbf{u}^{n+1} = \mathbf{u}^K$, $p^{n+1} = p^K$

It has been demonstrated [5] for the Stokes equations that the Uzawa algorithm converges under the condition $0 < \mathrm{d}p \leqslant 2\mathrm{d}r$. The use of high values of $\mathrm{d}r$ (up to $10^4$, $10^5$) increases the convergence



DOI: 10.1002/fld

of the algorithm but leads to ill-conditioned matrix associated to the discretization of the problem. Nevertheless, associated with a direct solver, this can be a judicious choice.

From a practical point of view, for the test cases described below, we have chosen $\mathrm{d}p = \mathrm{d}r$ and one to four iterations of the Uzawa algorithm. For a stationary problem, one iteration is enough, convergence being done on the time iterations. For unstationary problems, we have used four iterations at each time step to reach divergence level below $10^{-5}$.

Contrary to the time splitting methods, this algorithm does not even suffer from error introduced by the splitting of the operators. The precision of the method is only driven by the time and space schemes precisions. Finally, it has to be noted that no boundary condition is needed for the pressure, which is calculated explicitly in the whole domain.

Verifying the incompressible constraint at the computer precision can be expensive with regard to the CPU time. When the Uzawa algorithm is applied with few iterations, the resulting divergence of the velocity field is small but not identically null. To circumvent this drawback, we have used the vectorial projection method introduced by Caltagirone and Breil [18].

*2.1.2. Vectorial projection method.* Velocity $\mathbf{u}^{n+1}$ is decomposed into $\mathbf{u}^* + \mathbf{u}'$ where $\mathbf{u}^*$ is computed by the augmented Lagrangian step and is considered as a predictive divergence-free velocity. The latter verifies

$$\rho^n \left( \frac{\mathbf{u}^{n+1}}{\Delta t} + \nabla \cdot (\mathbf{u}^{n+1} \otimes \mathbf{u}^n) - \mathbf{u}^{n+1} \nabla \cdot \mathbf{u}^n \right) + \mathbf{BIU}(\mathbf{u}^{n+1} - \mathbf{u}_\infty)$$

$$= -\nabla p^n + \nabla \cdot \mu(\nabla \mathbf{u}^{n+1} + \nabla^{\mathrm{t}} \mathbf{u}^{n+1}) + \mathrm{d}r \nabla(\nabla \cdot \mathbf{u}^{n+1}) + \rho \frac{\mathbf{u}^n}{\Delta t} \tag{11}$$

By replacing $\mathbf{u}^{n+1}$ by $\mathbf{u}^* + \mathbf{u}'$ in (11), and with $\mathrm{d}r \to \infty$, we obtain

$$\nabla(\nabla \cdot \mathbf{u}^{n+1}) = \nabla(\nabla \cdot \mathbf{u}^*) + \nabla(\nabla \cdot \mathbf{u}') = 0 \tag{12}$$

or

$$\nabla(\nabla \cdot \mathbf{u}') = -\nabla(\nabla \cdot \mathbf{u}^*) \tag{13}$$

Both velocities $\mathbf{u}^{n+1}$ and $\mathbf{u}^*$ satisfy the physical boundary conditions. We deduce that the boundary conditions of $\mathbf{u}'$ are homogeneous.

The existence of the solution of the algebraic square system associated with Equation (13) is ensured by the fact that the second member is in the range of the discrete operator. In addition, one can check that the image is orthogonal to the kernel and thus their intersection is reduced to the null vector. The latter property makes possible to ensure the uniqueness of the solution, at least when the system is solved by an iterative method of Krylov type (BiCGStab in our case) while starting the iterative algorithm by an initial guess in the range of the operator (zero for example).

*2.1.3. Spatial discretization.* This is based on the finite volume method on velocity–pressure staggered grids of the Marker and Cells type [19]. Pressure unknowns are associated to the cell vertices, whereas velocity component are face centred. The centred scheme of order 2 is used in this work for the inertial and constraint terms.

A Dirichlet boundary condition on the normal component of the velocity field has to be verified on the pressure nodes which belong to the physical boundary. The existence of velocity points outside



DOI: 10.1002/fld

the domain requires to write the penalization term of the Navier–Stokes equations $\mathbf{BIU}(\mathbf{u}-\mathbf{u}_\infty)$ as $\mathbf{BIU}(\mathbf{f}_{\text{lim}}(\mathbf{u})-\mathbf{u}_\infty)$ where $\mathbf{f}_{\text{lim}}$ is a linear combination of the discrete unknowns (a centred scheme is used).

The linear system is sparse, composed of nine diagonals in 2D. The multifrontal spare direct solver MUMPS [20] is used to solve the Navier–Stokes linear system and a BiCGStab iterative solver, ILU preconditioned, is used for the linear system associated with the vectorial projection method.

### *2.2. On some domain decomposition methods*

In this numerical context, it is natural to be interested in domain decomposition techniques which offer a general framework for the treatment of block interfaces. Domain decomposition is based on the idea that the solution of a global problem can be obtained by assembling solutions of smaller, more regular ones. There are two fields of application: the first concerns the resolution of large linear systems, the second multiphysical problems (scale change, fluid/structure coupling, heterogeneous domains, etc.).

The principle of domain decomposition is quite simple. The domain is divided into sub-domains on which the original problem is written again in such a way that solutions are coupled thanks to appropriate conditions on the interfaces. Iterative techniques are usually used to solve the problem. The main example is the Dirichlet/Neumann algorithm for the Laplacian problem where the transmission condition connects the variables and their normal derivatives [21].

Generally speaking, domain decomposition deals with overlapping (or not) and conforming (or not) sub-domains. Historically, H. A. Schwarz was the originator of these techniques, with the additive and multiplicative algorithms. The main drawback of the Schwarz method is that overlapping is necessary for convergence. An improvement consists in replacing overlapping by a supplementary condition, the literature for which is very rich. The Dirichlet condition can be replaced by a Robin condition [22].

Our strategy is to work with overlapping. The challenge is then to find an adequate projection operator on the interfaces between the blocks. In this field, the mortar method has been proposed [23–25]. A method, based on the Robin condition, also deals with these problems [26, 27].

Another approach, the Chimera method [28, 29], is generally applied to aeronautical problems. Originally, this method aims to simplify mesh generation, coupling between blocks being achieved by an iterative Dirichlet/Dirichlet condition. Other interface conditions have also been proposed [30] (Dirichlet/Neumann, Dirichlet/Robin). Brezzi *et al.* [31] have proved that the Chimera method is a variant of the Schwarz algorithm.

Non-matching meshes raise the classical question of interpolation. This difficulty becomes important when it is necessary to interpolate under constraint (here $\nabla \cdot \mathbf{u} = 0$). The question is to know if precise and conservative operators exist. Generally, interpolation is conservative when it is based on finite volume techniques [32]. Fluxes (of mass, momentum or energy) through interfaces are calculated using local balance with a neighbouring block or a projection. Non-conservative interpolation is based on mathematical interpolation of the variables (Lagrange interpolation for instance). Some authors who use a non-conservative interpolation have shown that mass conservation is directly linked to the order of the interpolation method [33]. Although the conservative/non-conservative dilemma remains important, it has been minimized by Meakin [34]. According to him, what is important in the treatment of the interface is the sharpness of the grid. A precise non-conservative method can give better results than a less precise conservative one.



DOI: 10.1002/fld

*2.2.1. Towards an implicit connection between blocks.* We have chosen an implicit resolution of the conservation equations and the connecting conditions at the interface. The method is built on non-conservative interpolation of the variables. Polynomial coefficients are present in the global linear system and couple, at the same time, the solution both at each block and at the interfaces. This method can be seen as a non-iterative, implicit Dirichlet/Dirichlet condition for which minimal overlapping is necessary.

## 3. AN IMPLICIT METHOD FOR CONNECTING BLOCKS

Block-structured meshes allow a domain to be cut out according to the geometric contour. Generally, blocks have different orientations from one another, which induces a discontinuity of the mesh lines through the interfaces. We must connect the blocks by transferring the missing information from block to block. Polynomial interpolations are built and integrated as special boundary conditions in the global linear system. The proposed solution for transferring the information between blocks consists in implicitly interpolating a field $\phi$ at the nodes situated on the interfaces by using the nodes of the adjacent block. This interpolation can be considered as a new implicit boundary condition used for the discretization of the equation at the nodes strictly inside the different blocks (see Figure 1).

We will first present the method in the case of Cartesian blocks with parallel interfaces, then extend it to the case of Cartesian blocks of any orientation, and finally generalize it to curvilinear grids.

### 3.1. Parallel blocks

The variable $\phi$ ($u$ or $v$) defined on block (b) is interpolated, which gives the new boundary condition on block (a). We recall that the penalization term of the momentum equations used for the boundary conditions is written $\mathbf{BIU}(\mathbf{f}_{\lim}(\mathbf{u}) - \mathbf{u}_\infty)$. Here, the expression of $\mathbf{u}_\infty$ at the nodes of an interface is the result of the interpolation of the values of $\mathbf{u}$ on the adjacent block. The interpolation of the normal component of the velocity field to the interface is performed on pressure nodes, whereas velocity nodes are used for interpolating the tangential component (see Figure 2).

Interpolation is based on the construction of a polynomial basis of a given order. For instance, if $\phi$ represents $u$ or $v$, the interpolation of $\phi$ at a point $M_0(x_0, y_0)$ that belongs to a block (a) (or

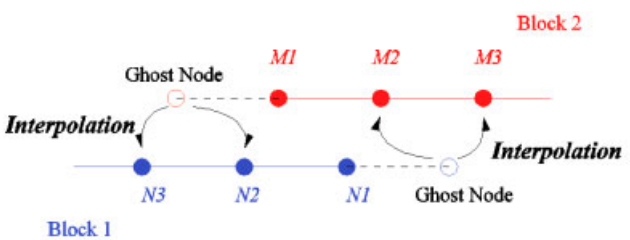


Figure 1. Connecting method for non-conforming meshes.



DOI: 10.1002/fld

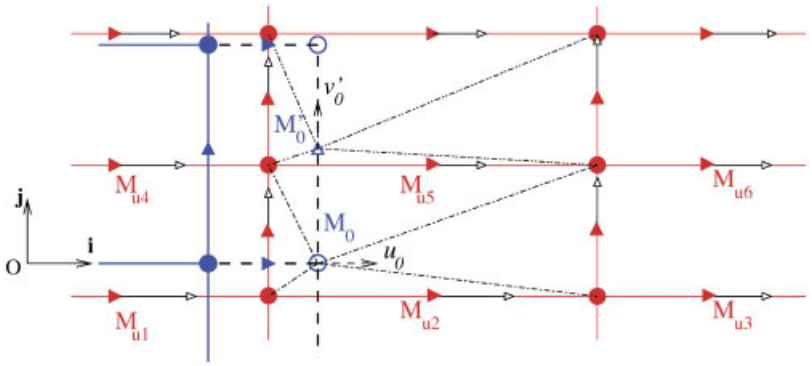


Figure 2. Interpolation of the velocity vector on a staggered grid.

at a point $M'_0(x_0, y_0)$ for $v$), is obtained from the values of $\phi$ on block (b) by the relation:

$$\phi^{(a)}(x_0, y_0) = f_{\text{int}}(\phi_i^{(b)}) = \sum_{i=1}^{N} F_i(x_0, y_0)\phi_i^{(b)}(x_i, y_i) \tag{14}$$

in which the $F_i$ are the values at the point $(x_0, y_0)$ of the $N$ polynomials that constitute the polynomial basis, and $\phi_i^{(b)}$ are the $N$ values of the field $\phi$ at the interpolation nodes $M_i(x_i, y_i)$ of block (b).

The interpolations must now be constructed locally to each node of the interface. The technique consists in building a canonical basis of $Q$-type polynomials of order $d$ thanks to the neighbouring nodes of $M_0(x_0, y_0)$. The number of nodes required depends on the order of the chosen polynomial.

In order to reduce the values of the coefficient of the polynomial, $M_0$ is chosen as the centre of the frame. A polynomial $Q_i^{(d)}$ built using the $M_i$ nodes, $1 \leqslant i \leqslant (d+1)^2$ is written

$$Q_i^{(d)}(x - x_0, y - y_0) = \sum_{m=0}^{d} \sum_{n=0}^{d} a_{mni}(x - x_0)^m (y - y_0)^n \tag{15}$$

It has the following properties:

$$\forall i, j, \quad 1 \leqslant i, \quad j \leqslant (d+1)^2, \quad Q_i^{(d)}(x - x_0, y - y_0) = \delta_{ij} \tag{16}$$

A $(d+1)^2 x (d+1)^2$ linear system is built (17), Equation (16) being a line of the matrix.

$$\begin{bmatrix} a_{001} & \cdot & a_{mn1} & \cdot & a_{dd1} \\ \cdot & & \cdot & & \cdot \\ a_{00i} & & a_{mni} & & a_{ddi} \\ \cdot & & \cdot & & \cdot \\ a_{00(d+1)} & \cdot & a_{mn(d+1)} & \cdot & a_{dd(d+1)} \end{bmatrix}, \quad B = \begin{bmatrix} 1 & \cdot & 0 & \cdot & 0 \\ \cdot & & \cdot & & \cdot \\ 0 & \cdot & 1 & \cdot & 0 \\ \cdot & & \cdot & & \cdot \\ 0 & \cdot & 0 & \cdot & 1 \end{bmatrix} \tag{17}$$



DOI: 10.1002/fld

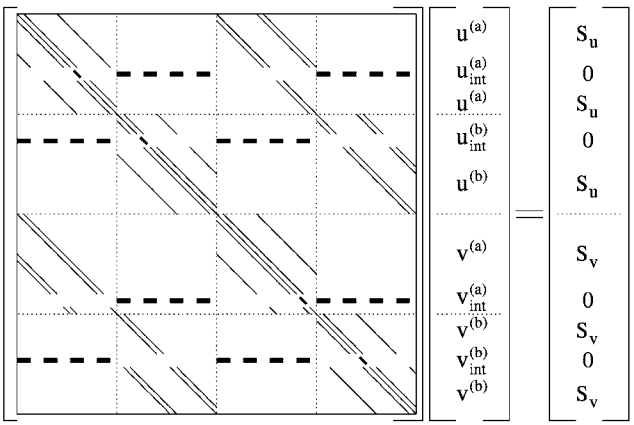


Figure 3. Representation of the Navier–Stokes matrix on 2 blocks.

with B given by

$$\begin{bmatrix} (x_1-x_0)^0(y_1-y_0)^0 & \cdot & (x_i-x_0)^0(y_i-y_1)^0 & \cdot & (x_{d+1}-x_0)^0(y_{d+1}-y_0)^0 \\ \cdot & & \cdot & & \cdot \\ (x_1-x_0)^m(y_1-y_0)^n & & (x_i-x_0)^m(y_i-y_1)^n & & (x_{d+1}-x_0)^0(y_{d+1}-y_0)^n \\ \cdot & & \cdot & & \cdot \\ (x_1-x_0)^d(y_1-y_0)^d & \cdot & (x_i-x_0)^d(y_i-y_1)^d & \cdot & (x_{d+1}-x_0)^0(y_{d+1}-y_0)^d \end{bmatrix} \tag{18}$$

The inversion of the linear system (one for each interface node) is carried out once during the preparation step of a simulation (before the time loop resolution). The value of the field $\phi$ at node $M_0(x_0, y_0)$ is then given by

$$\phi^{(a)}(x_0, y_0) = \sum_{i=1}^{(d+1)^2} Q_i^{(d)}(0,0)\phi^{(b)}(x_i, y_i) \tag{19}$$

It can be seen that the polynomial coefficients $Q_i^d(0,0)$ are not time dependent. By writing Equation (19) at time $n+1$, the $Q_i^{(d)}$ can be placed in the linear system (see Figure 3) of the momentum equations. Thus, on a matrix line corresponding to an interface node, non-zero elements are the main diagonal and the elements with a column number correspond to the unknowns used to interpolate the field.

### *3.2. Cartesian blocks with any orientation*

In the general case, the interface is not parallel to the mesh lines of the adjacent block. We consider now the case of two blocks (a) and (b) with non-collinear local frames $(i^{(a)}, j^{(a)})$ and $(i^{(b)}, j^{(b)})$ (see Figure 4). Both components of the velocity vector are thus necessary for the interpolation of each component. Frame changes are then required. As the velocity vector can be defined at



DOI: 10.1002/fld

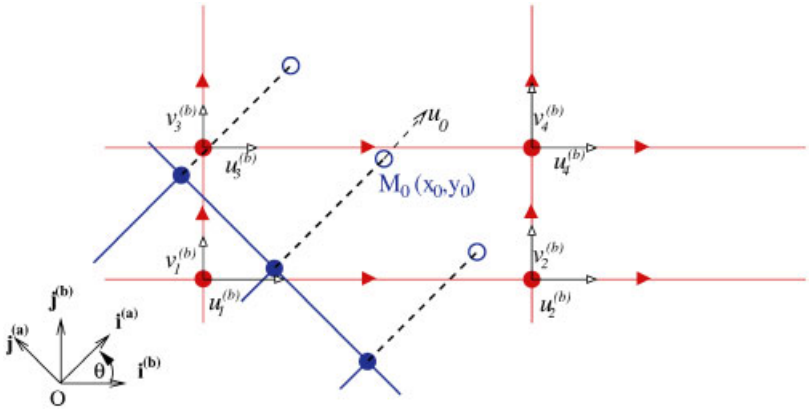


Figure 4. Interpolation of the velocity vector with frame change.

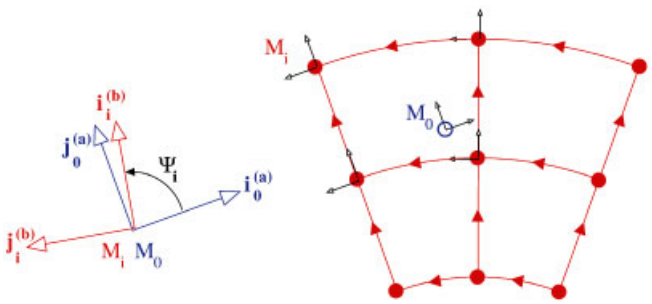


Figure 5. Interpolation of the velocity vector (curvilinear mesh).

the pressure node, the interpolation is performed at these nodes. Thus, for each component, the number of interpolations is doubled compared to the previous case:

$$\begin{aligned} u^{(a)}(x_0, y_0) &= \cos\theta \sum_{i=1}^{(d+1)^2} Q_i^{(d)}(0,0) u_i^{(b)}(x_i, y_i) - \sin\theta \sum_{i=1}^{(d+1)^2} Q_i^{(d)}(0,0) u_i^{(b)}(x_i, y_i) \\ v^{(a)}(x_0', y_0') &= \sin\theta \sum_{i'=1}^{(d+1)^2} Q_{i'}^{(d)}(0,0) v_{i'}^{(b)}(x_{i'}, y_{i'}) + \cos\theta \sum_{i'=1}^{(d+1)^2} Q_{i'}^{(d)}(0,0) v_{i'}^{(b)}(x_{i'}, y_{i'}) \end{aligned} \tag{20}$$

with $\theta$ the angle between the frames $(i^{(a)}, j^{(a)})$ and $(i^{(b)}, j^{(b)})$, and $u^{(b)}$, $v^{(b)}$ the velocity components at the pressure node.

### *3.3. Curvilinear blocks*

In the case of curvilinear blocks, the velocity field is defined on a local frame that is different at each point of the domain (see Figure 5).



DOI: 10.1002/fld

It is necessary to make frame changes locally to each node. Let $(i^{(a)}, j^{(a)})$ be the frame of an interface node. We have

$$\begin{aligned} u^{(a)}(x_0, y_0) &= \sum_{i=1}^{(d+1)^2} Q_i^{(d)}(0,0) u_0^{(b)}(x_i, y_i) \\ v^{(a)}(x_0', y_0') &= \sum_{i'=1}^{(d+1)^2} Q_{i'}^{(d)}(0,0) v_0^{(b)}(x_{i'}, y_{i'}) \end{aligned} \tag{21}$$

where $u_0^{(b)}$ and $v_0^{(b)}$ are expressed in the frame $(i^{(a)}, j^{(a)})$. The frame change from $(i^{(b)}, j^{(b)})$ to $(i^{(a)}, j^{(a)})$ gives

$$\begin{aligned} u_0^{(b)}(x_i, y_i) &= \cos(\psi_i) u_i^{(b)}(x_i, y_i) - \sin(\psi_i) v_i^{(b)}(x_i, y_i) \\ v_0^{(b)}(x_i', y_i') &= \sin(\psi_i) v_{i'}^{(b)}(x_{i'}, y_{i'}) + \cos(\psi_i) v_{i'}^{(b)}(x_{i'}, y_{i'}) \end{aligned} \tag{22}$$

We obtain

$$\begin{aligned} u^{(a)}(x_0, y_0) &= \sum_{i=1}^{(d+1)^2} Q_i^{(d)}(0,0) \cos(\psi_i) u_i^{(b)}(x_i, y_i) - \sin(\psi_i) v_i^{(b)}(x_i, y_i) \\ v^{(a)}(x_0', y_0') &= \sum_{i'=1}^{(d+1)^2} Q_{i'}^{(d)}(0,0) \sin(\psi_i) v_{i'}^{(b)}(x_{i'}, y_{i'}) + \cos(\psi_i) v_{i'}^{(b)}(x_{i'}, y_{i'}) \end{aligned} \tag{23}$$

Finally, the expression for the penalization term on an interface node is given by $\mathbf{BIU}(\mathbf{f}_{\text{lim}}(\mathbf{u}) - \mathbf{f}_{\text{int}}(\mathbf{u}))$, with

$$\mathbf{f}_{\text{int}}(\mathbf{u}) = \begin{pmatrix} \sum_{i=1}^{N} \alpha_{iu} u^{(2)}(x_i, y_i) + \sum_{j=1}^{N} \beta_{iu} v^{(2)}(x_i, y_i) \\ \sum_{i=1}^{N} \alpha_{iv} u^{(2)}(x_i, y_i) + \sum_{j=1}^{N} \beta_{iv} v^{(2)}(x_i, y_i) \end{pmatrix} \tag{24}$$

Coefficients $\alpha_{iu}$, $\alpha_{iv}$, $\beta_{iu}$ and $\beta_{iv}$ contain the expressions of frame changes, the values of interpolation polynomials, and the interpolation coefficients of the velocity on the pressure grid.

Pressure is also interpolated to ensure continuity of the pressure (to the order of the interpolation polynomial).

### *3.4. Mass conservation*

The non-conservative interpolation produces non-conservation of the mass between the blocks. Divergence is not null, especially at the interface nodes. We observe two behaviours: in the case of confined flows (driven cavity problem for instance), divergence levels are almost constant on each block; in the case of open flows (flow around a backward facing step, around a cylinder for instance), divergence is null on the whole domain except at the interface nodes. Even if, as we will see, the results of a series of test cases are good, this remains a drawback of the method. We propose to apply a correction to the method locally to each block, the mass non-conservation on the whole domain remaining unchanged.



DOI: 10.1002/fld

From the predictive velocity field $\mathbf{u}^*$ given by the Uzawa algorithm, we modify the boundary conditions associated with the vectorial projection method on each block using the Green–Ostrogradski formula (25) which links the integral of the velocity divergence over the whole block to the flow rate at the interface

$$\iiint_{\Omega_i} \nabla \cdot \mathbf{u}^* \, \mathrm{d}v = \iint_{\partial\Omega_i} \mathbf{u}^* \cdot \mathbf{n} \, \mathrm{d}s \tag{25}$$

The idea is to recover flow rate conservation on the boundary of each block by applying a velocity correction $\tilde{\mathbf{u}}^*$ such that

$$\iint_{\partial\Omega_i} (\mathbf{u}^* + \tilde{\mathbf{u}}^*) \cdot \mathbf{n} \, \mathrm{d}s = 0 \tag{26}$$

With Equation (25), we have

$$\iint_{\partial\Omega_i} \tilde{\mathbf{u}}^* \cdot \mathbf{n} \, \mathrm{d}s = - \iiint_{\Omega_i} \nabla \cdot \mathbf{u}^* \, \mathrm{d}v \tag{27}$$

The correction is applied only at the interfaces $\Gamma_i$ of each block because boundary conditions are already satisfied at the physical boundaries. Therefore, locally to each block, we have

$$\iint_{\Gamma_i} \tilde{\mathbf{u}}^* \cdot \mathbf{n} \, \mathrm{d}s = - \iiint_{\Omega_i} \nabla \cdot \mathbf{u}^* \, \mathrm{d}v = -D_{\Omega_i} \tag{28}$$

Thus, we can consider a homogeneous or a local correction at each interface node.

If $\tilde{\mathbf{u}}_l^*$ is the correction applied to the velocity $\mathbf{u}_l^*$ at an interface node, $\mathbf{n}_l$ the outward normal and $S_l$ the local section, the homogeneous correction is written

$$\tilde{\mathbf{u}}_l^* \cdot \mathbf{n}_l = \frac{D_{\Omega_i}}{\sum_{j=1}^{N} S_j} \tag{29}$$

And the local correction depending on the local flow rate is given by

$$\tilde{\mathbf{u}}_l^* \cdot \mathbf{n}_l = \frac{D_{\Omega_i} (\mathbf{u}_l^* \cdot \mathbf{n}_l S_l)}{S_j \sum_{j=1}^{N} \mathbf{u}_l^* \cdot \mathbf{n}_l S_j} \tag{30}$$

This correction can be applied to the vectorial projection method to ensure $\nabla \cdot (\mathbf{u}^* + \mathbf{u}') = 0$ locally to each block. The correction $\tilde{\mathbf{u}}^*$ is used to set a Dirichlet boundary condition on the interface (see Equation (31)). A few iterations of a BiCGStab with ILU preconditioning are enough to reach null divergence on each block.

**Solution of the augmented Lagrangian $\mathbf{u}^* = \mathbf{u}^{\mathbf{K}}$ and $\mathbf{p}^* = \mathbf{p}^{\mathbf{K}}$**
**Vectorial Projection**

- at each interface $\Gamma_i$ of section $S_i$ associated with a block $\Omega_i$, calculation of $\tilde{\mathbf{u}}'_{\infty i}$ from equation:

$$\tilde{\mathbf{u}}'_{\infty i} = - \frac{D_{\Omega_i}}{S_i} \mathbf{n}_i \tag{31}$$

- calculation of $\mathbf{u}'$ solution of:

$$\nabla(\nabla \cdot \mathbf{u}') + \mathbf{BIU}(\mathbf{f}_{\lim}(\mathbf{u}') - \tilde{\mathbf{u}}'_{\infty}) = - \nabla(\nabla \cdot \mathbf{u}^*)$$



DOI: 10.1002/fld

## 4. CONVERGENCE STUDY

### 4.1. Poiseuille flow (Cartesian meshes)

Simulations were carried out on the various block-structured meshes shown in Figure 6. Results are given for convergence criteria below $10^{-10}$ for stationarity.

With a $Q^1$ polynomial, the solution of Poiseuille flow, which is of order 2, cannot be reproduced without errors (see Table I). With $Q^2$ or $Q^3$ polynomials, errors are close to the computer accuracy.

### 4.2. Green–Taylor vortex

The main interest of this flow is that, unlike in Poiseuille flow, the inertial term is not null. The Green–Taylor vortex is modified to obtain a stationary solution not identically null. The momentum equations are enriched by the following source term:

$$\mathbf{S} = \begin{cases} -\dfrac{\pi^2 \mu}{2H^2} \cos\left(\dfrac{\pi x}{2H}\right) \sin\left(\dfrac{\pi y}{2H}\right) \\ -\dfrac{\pi^2 \mu}{2H^2} \sin\left(\dfrac{\pi x}{2H}\right) \cos\left(\dfrac{\pi y}{2H}\right) \end{cases} \tag{32}$$

The solution is

$$\begin{aligned} u(x, y, t) &= -\cos\left(\frac{\pi x}{2H}\right) \sin\left(\frac{\pi y}{2H}\right) (1 - \mathrm{e}^{-\pi^2 \upsilon t/2H^2}) \\ v(x, y, t) &= -\sin\left(\frac{\pi x}{2H}\right) \cos\left(\frac{\pi y}{2H}\right) (1 - \mathrm{e}^{-\pi^2 \upsilon t/2H^2}) \\ p(x, y, t) &= -\frac{\rho}{2} \left(\cos^2\left(\frac{\pi x}{2H}\right) + \cos^2\left(\frac{\pi y}{2H}\right)\right) (1 - 2\mathrm{e}^{-\pi^2 \upsilon t/2H^2} + \mathrm{e}^{-\pi^2 \upsilon t/H^2}) \end{aligned} \tag{33}$$

The boundary conditions are obtained directly from the analytical solution and are modified at each time step. The test case was run with two non-conforming structured blocks (see Figure 7).

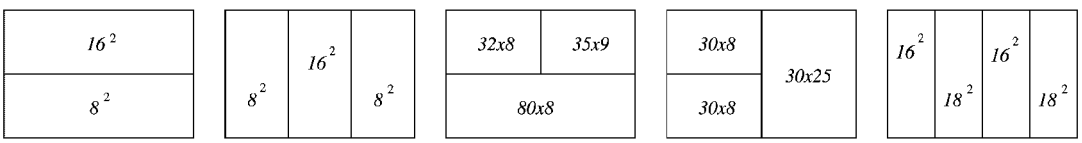


Figure 6. Representation of the different blocks for Poiseuille flow study; the number of elements per block is indicated.

Table I. $L_2$ norm of the error for Poiseuille flow.

| | Case 1 | Case 2 | Case 3 | Case 4 | Case 5 |
|---|---|---|---|---|---|
| $Q^1$ | $1.98 \times 10^{-3}$ | $7.81 \times 10^{-3}$ | $3.63 \times 10^{-2}$ | $2.05 \times 10^{-2}$ | $1.04 \times 10^{-3}$ |
| $Q^2$ | $1.02 \times 10^{-10}$ | $4.36 \times 10^{-13}$ | $3.18 \times 10^{-10}$ | $2.32 \times 10^{-12}$ | $4.15 \times 10^{-13}$ |
| $Q^3$ | $1.75 \times 10^{-10}$ | $2.71 \times 10^{-13}$ | $7.73 \times 10^{-9}$ | $30.3 \times 10^{-12}$ | $5.66 \times 10^{-13}$ |



DOI: 10.1002/fld

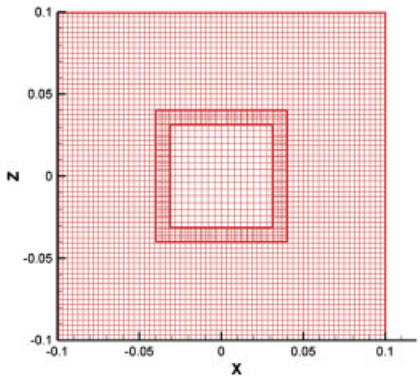


Figure 7. Block-structured mesh example for the Green–Taylor flow study.

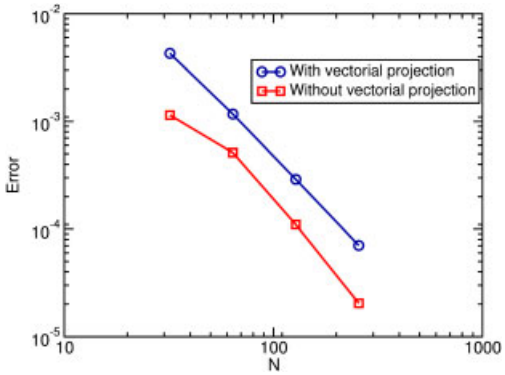


Figure 8. $L_2$ norm of the error as a function of mesh size for the Green–Taylor flow study.

Table II. $L_\infty$ norm of the error on velocity field at $T = 1$ s.

| $\Delta t$ (s) | 0.1 | 0.05 | 0.01 | 0.005 | 0.001 |
|---|---|---|---|---|---|
| $L_\infty$ error | $7.72 \times 10^{-4}$ | $3.87 \times 10^{-4}$ | $7.93 \times 10^{-5}$ | $4.08 \times 10^{-5}$ | $1.00 \times 10^{-5}$ |
| Local slope (in log/log scale) | | 0.99 | 0.98 | 0.96 | 0.87 |

The domain is a square of side length 0.2 m ($H = 0.1$). The fluid used has a density of $1.176\,\mathrm{kg/m^3}$ and a viscosity of $1.85 \times 10^{-5}$ Pa s.

Simulations were performed using or not using the vectorial projection method. We first focus on the stationary solution. With $Q^2$ interpolation polynomials, the spatial convergence order is two, as shown in Figure 8. Validation on pressure was not established. Indeed, divergence at the end of the Uzawa algorithm was not null (around $10^{-6}$) and accumulated in the pressure.

Then, a time convergence study has been carried out (a two blocks non-conforming mesh size of 4300 nodes is used). Errors on velocity field at time $T = 1$ s are presented in Table II. Local



DOI: 10.1002/fld

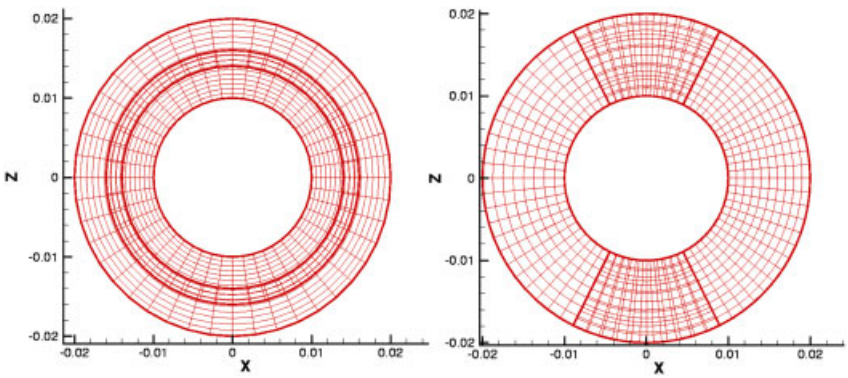


Figure 9. Block-structured curvilinear meshes.

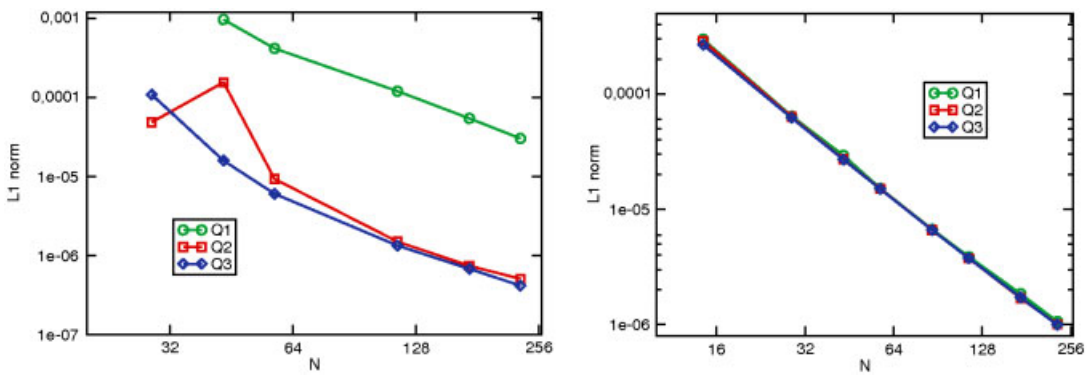


Figure 10. Convergence order for radial flow; radial (left) and polar (right) sections.

slope in a log/log scale gives a time convergence order of one, coherent with the scheme used (Euler time scheme and linearization at order 1). With very small time step, the stagnation of the error is due to the saturation of the time error by the spatial one.

### *4.3. Couette and radial flows (curvilinear meshes)*

In order to validate the method on 2D curvilinear meshes, we studied the spatial convergence order on two academic cases (Couette and radial flows) based upon two structured non-conforming blocks (see Figure 9). The interfaces can be along the radius or at a constant angle (radial or polar section).

Results are presented for each type of section and for $Q^1$, $Q^2$ and $Q^3$ interpolation polynomials. The $L_1$ norm of the error compared to the analytical solution was chosen to represent the order of convergence.

As shown in Figures 10 and 11, the spatial convergence order is 2 whatever the polynomial used. We note that the level of errors obtained with the $Q^1$ polynomial is higher than for the $Q^2$ and $Q^3$ polynomials.



DOI: 10.1002/fld

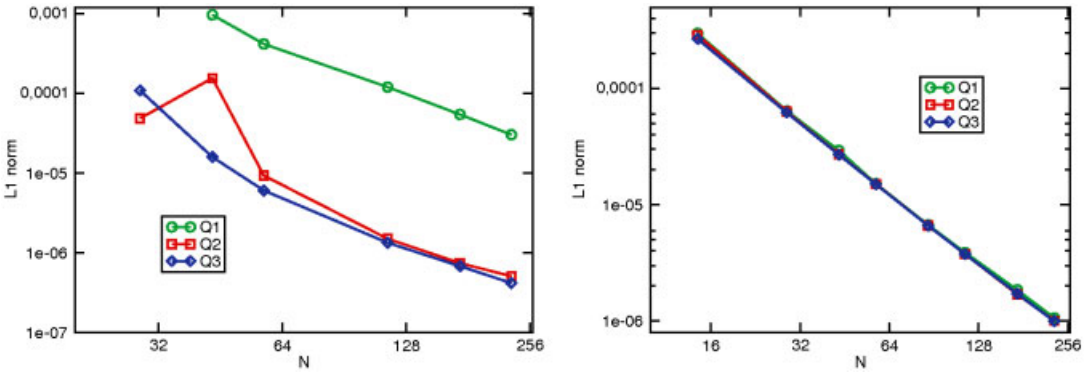


Figure 11. Convergence order for Couette flow; radial (left) and polar (right) cutting.

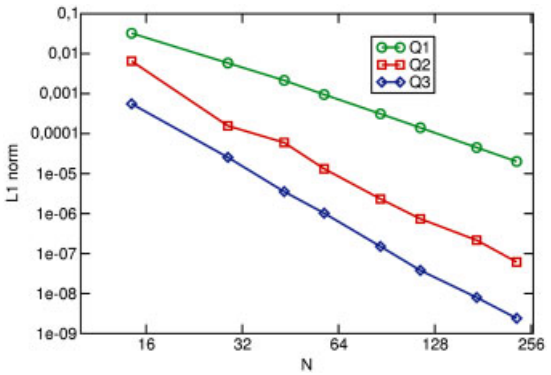


Figure 12. $L_1$ norm of the velocity divergence for radial flow (polar section).

### *4.4. Conclusion on the convergence order of the method*

Generally speaking, it can be observed that the spatial convergence order of the code is not deteriorated by the interpolation. The $Q^1$ polynomial is not really interesting because error levels are too high. The $Q^3$ polynomial is not of a great interest: error levels are slightly lower than with the $Q^2$ polynomial but they need many more points to interpolate. Moreover, velocity divergence levels are also dependent on the order of interpolation (see Figure 12). For the further simulations, we chose the $Q^2$ polynomial because it was a good compromise between error level, velocity divergence and ease of implementation.

## 5. NUMERICAL SIMULATIONS

### *5.1. Driven cavity ($Re = 1000$)*

*5.1.1. Description of the test case.* Since the early work of Burggraf [35], lid-driven cavity flow has been considered as a classic test problem for the assessment of numerical methods and the



DOI: 10.1002/fld

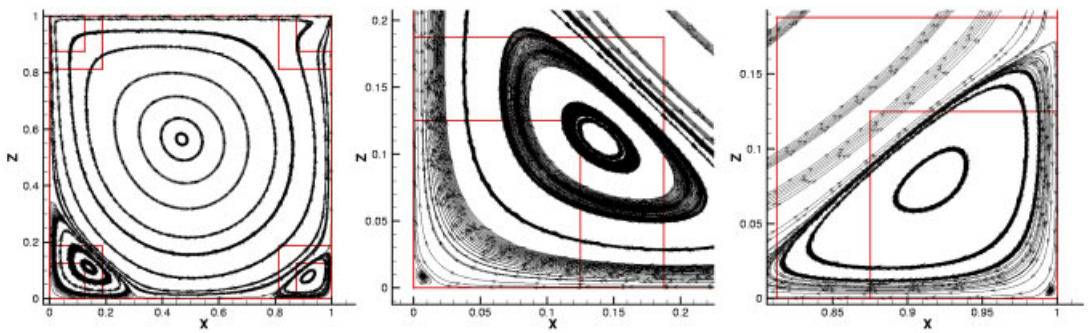

Figure 13. Streamlines of the driven cavity flow.

Table III. Comparison of the intensity and the position $(x, y)$ of the main vortex.

| Reference | Mesh size | Maximum streamline | $X$ | $Y$ |
|---|---|---|---|---|
| Aq. block-structured | 121 344 ($\approx 348^2$) | 0.11877 | 0.4687 | 0.5664 |
| Aq. monoblock | $512^2$ | 0.11893 | 0.4693 | 0.5642 |
| Botella and Peyret | $512^2$ | 0.11894 | 0.4692 | 0.5652 |
| Bruneau | $256^2$ | 0.1163 | 0.4687 | 0.5586 |
| Barragy *et al.* | $256^2$ | 0.11893 | — | — |
| Schreiber *et al.* | $141^2$ | 0.11603 | 0.4714 | 0.5643 |
| Ghia *et al.* | $128^2$ | 0.11793 | 0.4687 | 0.5625 |

validation of CFD codes. In the present article, we refer to the work of Botella and Peyret [36]. Their article is a benchmark rich in References [37–40], for which the main results are given for the singular driven cavity flow at a Reynolds number of 1000. The upper boundary tangential velocity leads to the formation of a main vortex that fills the main part of the cavity. In the lower corners, secondary and ternary vortices appear (see Figure 13).

The mesh is divided into five structured blocks (see Figure 13): the first block occupies the main part of the domain; the two lower (upper) blocks have step spaces a third (half) the size of the main block. There are 121 344 elements ($\approx 256 \times 256$ on the main block, $64 \times 64$ for an upper block and $96 \times 96$ for a lower one). In this case, the block-structured mesh is used to refine the description of the flow in the corners of the domain.

The main results found in the literature are given on the intensity and position of the vortices. Our results are obtained with convergence criteria on stationarity below $10^{-12}$. We also present results obtained on a monoblock mesh with a Chebychev polynomial step size variation.

*5.1.1.1. Position and intensity of the vortices.* The results presented in Tables III–VII show a good correlation between our values and those of other authors.

*5.1.1.2. Velocity and pressure profile.* Figures 14 and 15 show comparisons of the velocity profiles between monoblock, block-structured and those obtained by Bottela and Peyret [36].



DOI: 10.1002/fld

Table IV. Comparison of the intensity and the position $(x, y)$ of the left secondary vortex.

| Reference | Mesh size | Maximum streamline | $X$ | $Y$ |
|---|---|---|---|---|
| Aq. block-structured | 121 344 ($\approx 348^2$) | $-1.7285 \times 10^{-3}$ | 0.1354 | 0.1120 |
| Aq. monoblock | $512^2$ | $-1.7314 \times 10^{-3}$ | 0.1358 | 0.1116 |
| Botella and Peyret | $512^2$ | $-1.7297 \times 10^{-3}$ | 0.1360 | 0.1118 |
| Bruneau | $256^2$ | $-1.91 \times 10^{-3}$ | 0.1289 | 0.1094 |
| Schreiber *et al.* | $141^2$ | $-1.7 \times 10^{-3}$ | 0.1357 | 0.1071 |
| Ghia *et al.* | $128^2$ | $-1.7210 \times 10^{-3}$ | 0.1406 | 0.1094 |

Table V. Comparison of the intensity and the position $(x, y)$ of the right secondary vortex.

| Reference | Mesh size | Maximum streamline | $X$ | $Y$ |
|---|---|---|---|---|
| Aq. block-structured | 121 344 ($\approx 348^2$) | $-2.3481 \times 10^{-4}$ | 0.9167 | 0.0781 |
| Aq. monoblock | $512^2$ | $-2.3347 \times 10^{-4}$ | 0.9157 | 0.0776 |
| Botella and Peyret | $512^2$ | $-2.3345 \times 10^{-4}$ | 0.9167 | 0.0781 |
| Bruneau | $256^2$ | $-3.25 \times 10^{-4}$ | 0.9141 | 0.0820 |
| Schreiber *et al.* | $141^2$ | $-2.17 \times 10^{-4}$ | 0.9143 | 0.0714 |
| Ghia *et al.* | $128^2$ | $-2.3113 \times 10^{-4}$ | 0.9141 | 0.0781 |

Table VI. Comparison of the intensity and the position $(x, y)$ of the left ternary vortex.

| Reference | Mesh size | Maximum streamline | $X$ | $Y$ |
|---|---|---|---|---|
| Aq. block-structured | 121 344 ($\approx 348^2$) | $-4.7314 \times 10^{-8}$ | 0.00781 | 0.00781 |
| Aq. monoblock | $512^2$ | $-5.0239 \times 10^{-8}$ | 0.00789 | 0.00736 |
| Botella and Peyret | $512^2$ | $-5.0399 \times 10^{-8}$ | 0.00768 | 0.00765 |
| Ghia *et al.* | $128^2$ | $-9.3193 \times 10^{-8}$ | 0.0078 | 0.0078 |

Table VII. Comparison of the intensity and the position $(x, y)$ of the right ternary vortex.

| Reference | Mesh size | Maximum streamline | $X$ | $Y$ |
|---|---|---|---|---|
| Aq. block-structured | 121 344 ($\approx 348^2$) | — | 0.9952 | 0.00463 |
| Aq. monoblock | $512^2$ | $6.3462 \times 10^{-9}$ | 0.9950 | 0.00497 |
| Botella and Peyret | $512^2$ | $6.33255 \times 10^{-9}$ | 0.9951 | 0.00482 |
| Bruneau | $128^2$ | $3.06 \times 10^{-9}$ | 0.9961 | 0.0039 |

Small differences on velocity profiles between the monoblock and block-structured solutions can be explained by grid resolution differences. As regards the pressure profiles (see Figure 16), good agreement can be observed with those obtained with a monoblock mesh, except on the interface of the upper blocks. The overpressure (depression) observed in the upper right (upper left) block is the result of the velocity divergence levels, which are constant in each block (around $10^{-5}$). We did not observe these phenomena on other test cases presented in this paper where pressure



DOI: 10.1002/fld

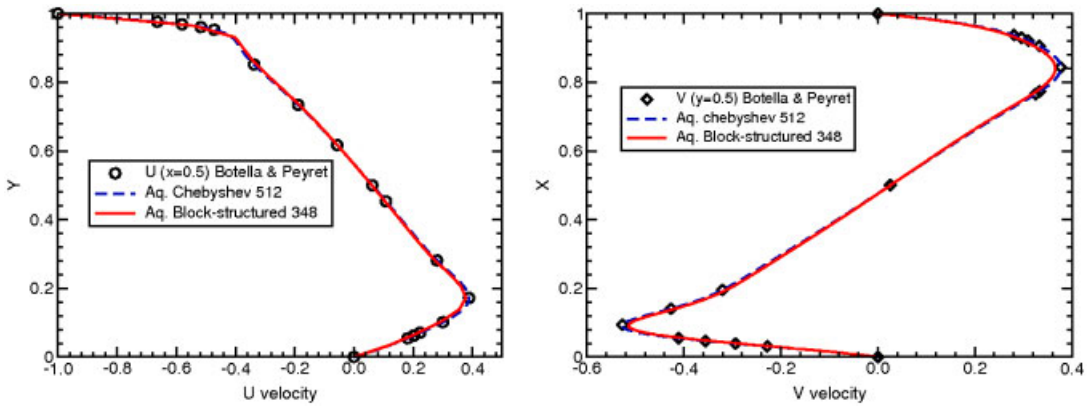


Figure 14. $U$ profiles (left) at $X = 0.5$ and $V$ profiles (right) at $Y = 0.5$.

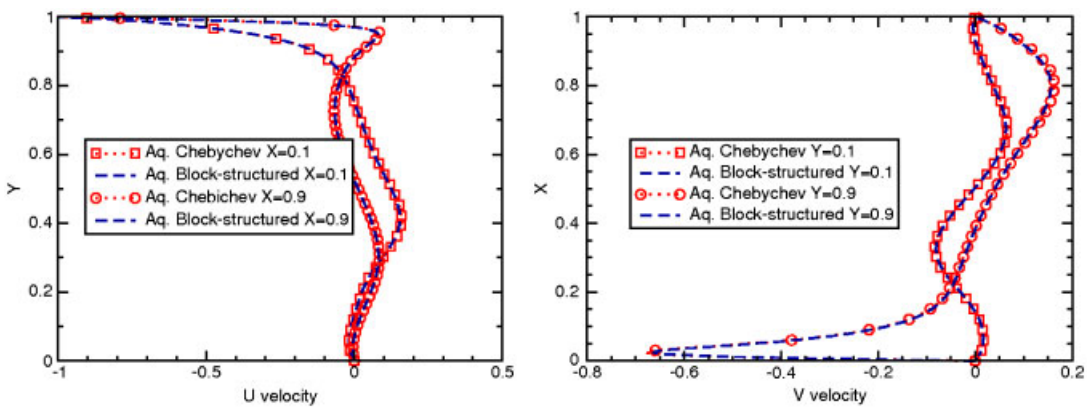


Figure 15. $U$ profile (left) at $X = 0.1$ and 0.9. $V$ profile (right) at $Y = 0.1$ and 0.9.

was continuous through the interfaces. There is no doubt that a Neumann condition relaxes the constraint through the different blocks. When the domain is closed, a lack of conservation of mass and momentum due to interpolation explain the pressure shift observed.

### 5.2. *Flow around a backward facing step* ($Re \leqslant 1000$)

*5.2.1. Description of the test case.* The backward-facing step is one of the most fundamental examples where laminar separation is caused by the sudden change in the geometry. The extension of the section induces a reverse pressure gradient that leads to a separation of the flow into several zones: a recirculation appears behind the step and, when the Reynolds number increases, a second recirculation appears on the upper wall. The experimental reference works are those of Armaly *et al.* [41] and, to a lesser degree, the work of Lee and Matescu [42]. The Reynolds number, based on the height of the channel $H_d$, the bulk velocity at the entrance of the channel $U_{moy}$ and the kinematic viscosity, vary between 100 and 1000.



DOI: 10.1002/fld

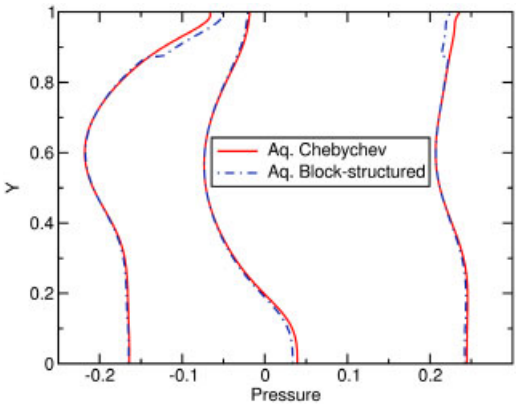


Figure 16. Pressure profiles at $X = 0.1$, 0.5 and 0.9.

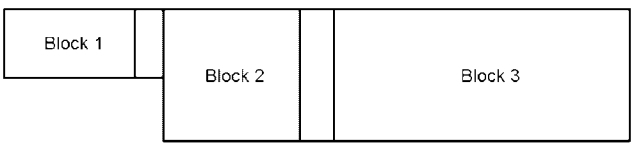


Figure 17. Block-structured mesh for the backward-facing step flow.

Armaly's experiments were performed on a channel of width equal to 36.7 times the step height. Flow can be considered as 2D below $Re = 400$, wall effects being not negligible for higher Reynolds numbers. Comparisons between the experiments and the results of other authors were made on the detachment and reattachment positions.

In the present work, we used a monoblock mesh and a block-structured one (see Figure 17): the domain was divided into three blocks, the middle one being twice as fine as the others. The interface between block 2 and block 3 was positioned at the middle of the recirculation, at a distance of 6.5 m from the step foot (see Figure 18).

We will compare the results obtained using two non-conforming meshes (3456 and 24 576 elements) with those obtained with a monoblock mesh and those of several other authors. The stationarity criterion was set to $10^{-10}$ whatever the Reynolds number. We have separated the results in two parts: for $Re \leqslant 400$ and for $Re > 400$. In the first case, there is no upper recirculation and 3D effects are negligible.

*5.2.1.1. Lower recirculation $Re \leqslant 400$.* Agreement with the experiments and various numerical results [15, 43–45] is very good as shown in Figure 19.

These results were obtained without the vectorial projection method. Velocity divergence is null over the whole domain except at the interface node where it is around $10^{-4}$ due to the non-conservative interpolation. We performed other simulations with the vectorial projection method. Therefore, divergence is null on the interface without any strong influence on the recirculation length as shown in Table VIII.



DOI: 10.1002/fld

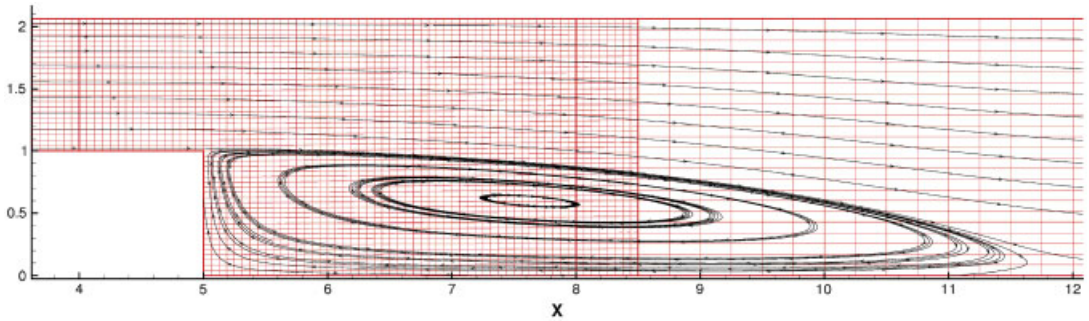


Figure 18. Streamlines through the interfaces ($Re = 500$).

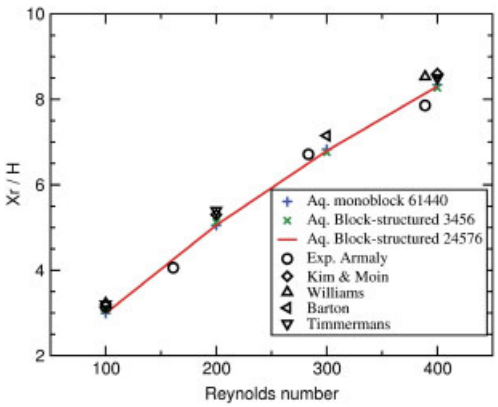


Figure 19. Recirculation length ($X_r/H$) for $Re \leqslant 400$. $X_r$ is the length of the lower recirculation and $H$ the step height.

Table VIII. Influence of the vectorial projection method on the recirculation length ($Re \leqslant 400$).

| $Re$ | 100 | 200 | 300 | 400 |
|---|---|---|---|---|
| Recirculation length | 2.99 | 5.06 | 6.79 | 8.30 |
| Correction in % | $4.3 \times 10^{-2}$ | $2.3 \times 10^{-1}$ | $4.2 \times 10^{-2}$ | $5.1 \times 10^{-2}$ |

*5.2.1.2. Lower recirculation for Re>400.* The upper recirculation appears and the reattachment point of the lower recirculation continues to move off the foot of the step. The experimental results of Armaly and Lee are quite different (see Figure 20). If we compare our results to those of Armaly, the length of the lower recirculation is underestimated with an error of 8.6% by the monoblock mesh and 9% by the block-structured one at $Re = 500$. At $Re = 1000$, errors are around 19%. Williams and Baker [45] have shown with a 3D simulation that these differences are due to 3D effects. Indeed, most other 2D numerical studies found in the literature [43–47] show the same order of error (see Figure 20 and Table IX).



DOI: 10.1002/fld

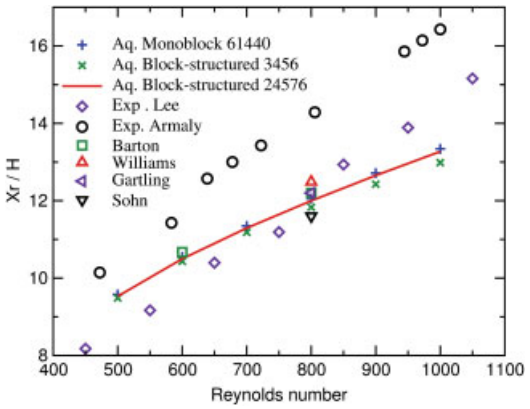


Figure 20. Lower recirculation length ($X_r/H$) for $Re>400$.

Table IX. Lower recirculation length, $Re=800$.

| | Lee | Armaly | Aq. monoblock | Aq. block-structured | Lee | Gartling | Kim | Sohn |
|---|---|---|---|---|---|---|---|---|
| $X_r$ | 12.9 | 14.2 | 12.05 | 11.99 | 12 | 12.2 | 12 | 11.6 |

Table X. Influence of the correction on the lower recirculation length ($Re>400$).

| *Re* | 500 | 600 | 700 | 800 | 900 | 1000 |
|---|---|---|---|---|---|---|
| Recirculation length | 9.53 | 10.50 | 11.29 | 12 | 12.65 | 13.28 |
| Correction in % | $4.2\times10^{-2}$ | $7.6\times10^{-3}$ | $4.4\times10^{-3}$ | $1.7\times10^{-2}$ | $1.9\times10^{-2}$ | $2.4\times10^{-2}$ |

Finally, Table X shows very low differences if we use the vectorial projection method to reach null divergence over each block.

*5.2.1.3. Upper recirculation for Re>400.* The abscissa of the detachment point on the upper wall is underestimated, from $Re=600$, compared to the results of Armaly (see Figure 21 left). Compared to the Lee's results, it is overestimated until $Re=750$ and then underestimated. Again, 3D effects explain these differences. They are less obvious if one looks at the abscissa of the upper reattachment point (see Figure 21 right).

It must be noted that the length of the upper recirculation at $Re=800$ is overestimated by around 18% with a monoblock mesh and by 15% with a block-structured one. As noted by Armaly, the lengths of the lower and the upper recirculations are strongly coupled, an underestimation of one of them involving an overestimation of the other. Our results are in agreement with other numerical studies found in the literature (see Table XI).

The flow rate difference between the entrance and the exit of the domain is around $6.10^{-4}$ m$^3$ s$^{-1}$ whatever the Reynolds number. The non-conservative interpolation finally has little influence on the accuracy of the results. Velocity divergence on the interface between the blocks is relatively small, and decreases with mesh refinement as shown in Figure 22.



DOI: 10.1002/fld

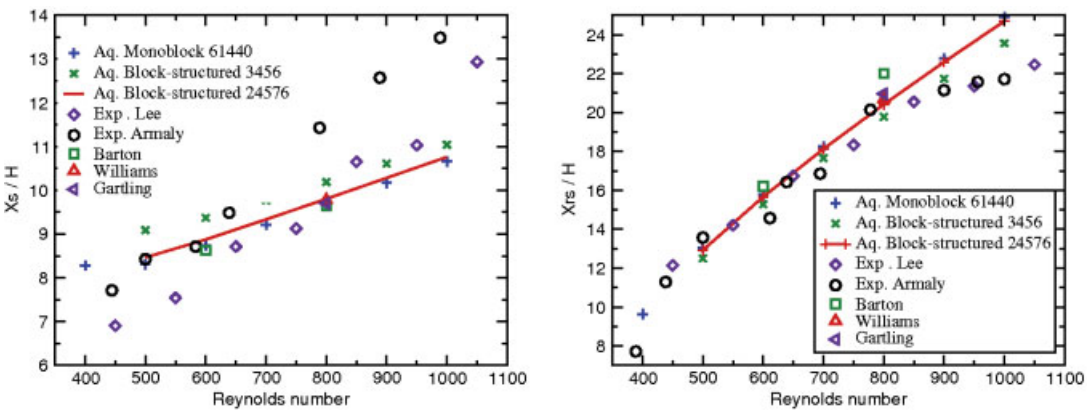


Figure 21. Abscissae of the detachment ($X_s$) and reattachment ($X_{rs}$) points *versus* Reynolds number.

Table XI. Comparison of the abscissae of the detachment and reattachment points at $Re = 800$.

| | Exo. Lee | Exp. Armaly | Aq. monoblock | Aq. block-structured | Lee | Gartling | Kim | Sohn |
|---|---|---|---|---|---|---|---|---|
| $X_S$ | 10.3 | 11.5 | 9.69 | 9.80 | 9.6 | 9.7 | — | — |
| $X_{rs}$ | 19.5 | 20 | 20.57 | 20.41 | 20.6 | 20.96 | — | — |
| $X_{rs} - X_s$ | 9.2 | 8.5 | 10.88 | 10.61 | 11 | 11.26 | 11.5 | 9.26 |

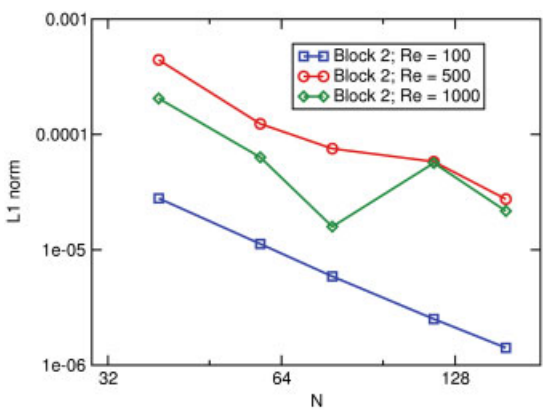


Figure 22. Mean divergence on the block interface as a function of the mesh size for different Reynolds numbers.

Figure 23 shows several velocity profiles and a good agreement between the monoblock and the block-structured solutions. The non-conservative interpolation does not produce significant differences with conforming meshes.



DOI: 10.1002/fld

### 5.3. *Flow around a cylinder*

The flow around a cylinder has been widely studied from the theoretical, experimental and numerical points of view. The problem can be characterized by the Reynolds number, based on the diameter of the cylinder and the entrance velocity. We are interested in two flow ranges:

- $4<Re<49$: the inertial term of the momentum is not negligible. One can observe a detachment of the streamlines around the cylinder and the presence of two symmetrical, stable vortices, the lengths which increase with the Reynolds number.
- $49<Re<190$: the flow is not stationary. The result is a Von Karman alley with alternating vortex detachment, the frequency of which increases with the Reynolds numbers characterized by the Strouhal number.

*5.3.1. Parameters of the test case.* To validate our method, we studied the length of the recirculation; the detachment angle and the drag coefficient $C_x$ for Reynolds numbers below 49. We compared our results with the experimental work of Taneda [48], Tritton [49], Acrivos *et al*. [50], Coutanceau and Bouard [51], and with the numerical works of Dennis and Chang [52], Nieuwstadt and Keller [53], Fornberg [54] and, more recently, He and Doolen [55]. For higher Reynolds number, we compared our results on the Strouhal number to the law of Williamson and Brovon [56], which is in good agreement with experiments.

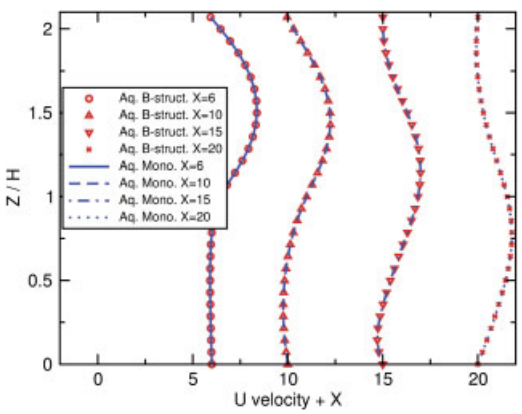


Figure 23. $u$ component profiles for monoblock and block-structured meshes at $Re = 800$.

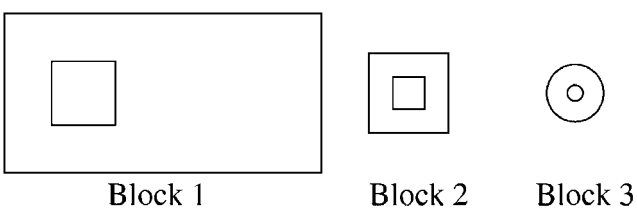


Figure 24. Block-structured mesh composition for the study of the flow around a cylinder.



DOI: 10.1002/fld

Table XII. Recirculation length, detachment angle and drag coefficient at $Re = 10$.

| Authors | $L/r$ | $\theta_d$ | $C_x$ |
|---|---|---|---|
| Aq. block-structured | 0.549 | 25.47 | 3.077 |
| Dennis and Chang [52] | 0.53 | 29.6 | 2.846 |
| Nieuwstadt and Keller [53] | 0.434 | 27.96 | 2.828 |
| Coutanceau and Bouard [51] | 0.68 | 32.5 | — |
| He and Doolen [55] | 0.474 | 26.89 | 3.170 |

Table XIII. Recirculation length, detachment angle and drag coefficient at $Re = 20$.

| Authors | $L/r$ | $\theta_d$ | $C_x$ |
|---|---|---|---|
| Aq. block-structured | 2.16 | 41.98 | 2.070 |
| Dennis and Chang [52] | 1.88 | 43.7 | 2.045 |
| Nieuwstadt and Keller [53] | 1.786 | 43.37 | 2.053 |
| Coutanceau and Bouard [51] | 1.86 | 44.8 | — |
| Fornberg [54] | 1.82 | — | 2.000 |
| He and Doolen [55] | 1.842 | 42.96 | 2.152 |

Table XIV. Recirculation length, detachment angle and drag coefficient at $Re = 30$.

| Authors | $L/r$ | $\theta_d$ | $C_x$ |
|---|---|---|---|
| Aq. block-structured | 3.57 | 47.93 | 1.702 |
| Nieuwstadt and Keller [53] | 3.09 | — | 1.716 |

Table XV. Recirculation length, detachment angle and drag coefficient at $Re = 40$.

| Authors | $L/r$ | $\theta_d$ | $C_x$ |
|---|---|---|---|
| Aq. block-structured | 4.94 | 50.99 | 1.503 |
| Dennis and Chang [52] | 4.69 | 53.8 | 1.522 |
| Nieuwstadt and Keller [53] | 4.357 | 53.34 | 1.550 |
| Coutanceau and Bouard [51] | 4.26 | 53.5 | — |
| Fornberg [54] | 4.48 | — | 1.498 |
| He and Doolen [55] | 4.490 | 52.84 | 1.499 |
| Prabhakar [57] | 4.55 | — | 1.55 |

Figure 24 shows the block-structured mesh composition we used. It is based on the superposition of three blocks: the first two are Cartesian blocks with a hole, the last one is a disk. Space step size becomes increasingly thin. The total number of elements is 33 168. Around the cylinder of diameter 1, there are 240 elements according to $\theta$, and space step size in the $r$ direction is 0.25 m.

*5.3.2. Stationary flow $4<Re<49$.* As shown in Tables XII–XV, the recirculation length is generally overestimated compared to other numerical results found in the literature. The error reaches 26%



DOI: 10.1002/fld

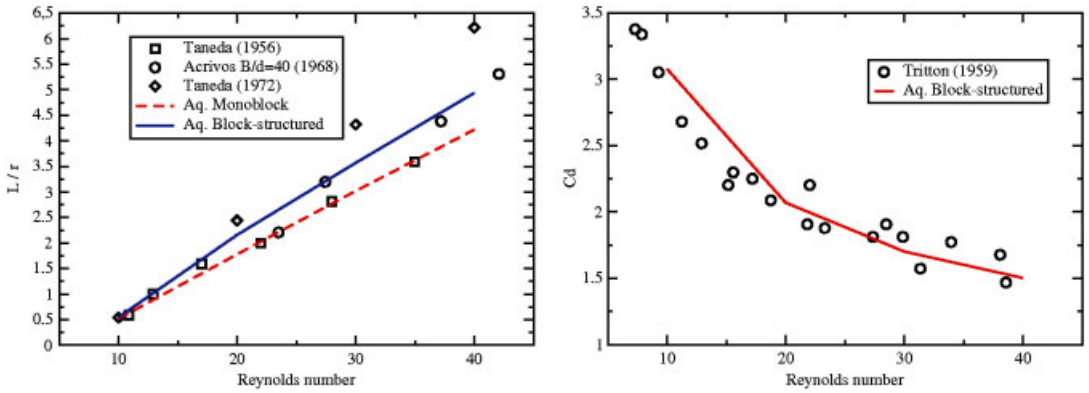


Figure 25. Recirculation length (left) and drag coefficient (right) *versus* the Reynolds number.

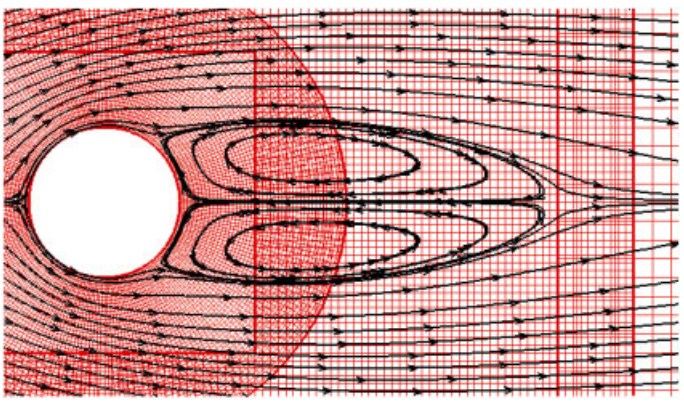

Figure 26. Streamlines of the flow around a cylinder at $Re = 40$.

Table XVI. Strouhal number at various Reynolds numbers.

| *Re* | Block-structured | Williamson |
|---|---|---|
| 80 | 0.158 | 0.155 |
| 100 | 0.170 | 0.166 |
| 120 | 0.180 | 0.175 |
| 140 | 0.185 | 0.182 |
| 160 | 0.192 | 0.188 |

with respect to Nieuwstadt and Keller [53] at $Re = 10$. Differences decrease with the increase of the Reynolds number (around 10% at $Re = 40$). Nevertheless, our values are in the uncertainty area of the experiment (see Figure 25 left). The same comments can be made regarding the detachment angle. Results obtained on the drag coefficient (see Figure 25 right) are much closer to those found in the literature. Figure 26 shows the mesh and the streamlines around the cylinder and through the interfaces.



DOI: 10.1002/fld

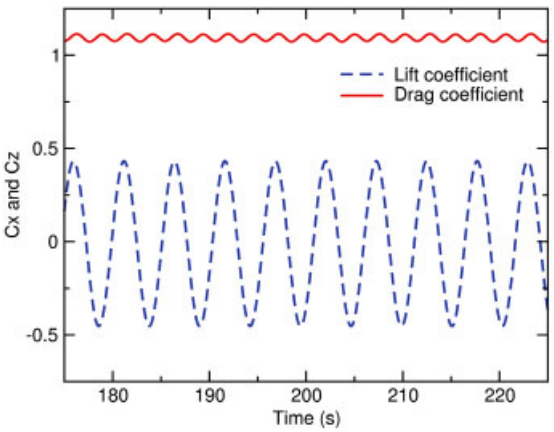


Figure 27. Drag and lift coefficients at $Re = 160$.

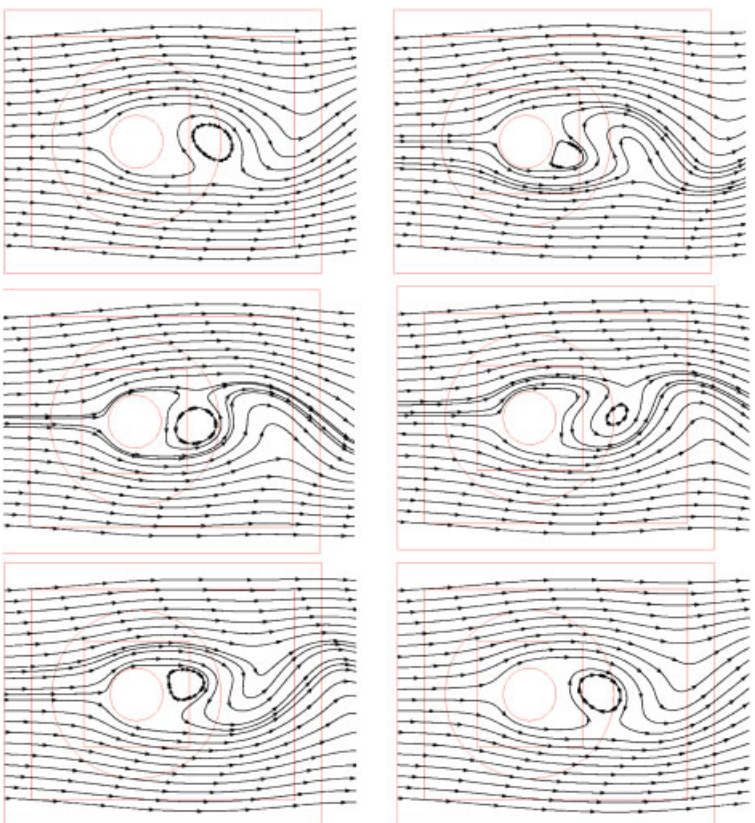

Figure 28. Streamlines of the flow around a cylinder during a period at $Re = 160$.



DOI: 10.1002/fld

*5.3.3. Unstationary flow 49<Re<190.* As shown in Table XVI, results are very close to the Williamson Strouhal law. The overestimation is around 3%. At $Re = 160$, Figures 27 and 28 show the time variation of the lift and drag coefficients and the streamlines around the cylinder during a period.

## 6. CONCLUSION

In the present work, we have proposed and validated a connecting technique for non-conforming and overlapping block-structured meshes. It is non-iterative and based on an implicit non-conservative interpolation. This is performed in the context of the augmented Lagrangian method and the iterative Uzawa algorithm. The linear system of the Navier–Stokes equations is modified: lines that correspond to the interface nodes link the blocks together. Thus, the discretization of the equations and the connecting conditions are implicit.

With a series of test cases for which the analytical solution is known, we have demonstrated that the spatial convergence order is 2. Numerical simulations of laminar and incompressible flows show the feasibility and validity of the method.

Nevertheless, the interpolation used does not allow the incompressibility constraint to be fully attained over the whole domain. The problem of mass conservation through the interface remains. This problem is altogether logical because the interpolation acts as a Dirichlet condition on the interfaces.

We have modified the vectorial projection method to ensure mass conservation locally to each block. New conditions on the interfaces have been written that take into account the flow rate difference at each interface between blocks. In particular cases, it could be possible to take into account the flow rate difference between blocks or to bring each block flow rate to a reference one (to the entrance flow rate for instance). In the future, it will be necessary to connect gradient-type information between the blocks (normal constraint) to ensure a better conservation of the momentum and the incompressible constraint. The main difficulty to be dealt with lies in the implicit treatment of this new condition.

ACKNOWLEDGEMENTS

We acknowledge the reviewers for their valuable contributions which have been of great help in improving the quality of the presentation and discussion of the results. The authors thank Professor Mejdi Azaïez for his critical reading, helpful suggestions and fruitful discussions that guided us to achieve this work. We acknowledge calculation facilities provided by the 'M3PEC-Mésocentre Régional' main frame supercomputers of the University Bordeaux 1 financed by the University, the 'Conseil Régional d'Aquitaine' and the French Ministry of Research and Technology.

REFERENCES

1. Romé C, Glockner S. An implicit multiblock coupling for the incompressible Navier–Stokes equations. *International Journal for Numerical Methods in Fluids* 2005; **47**:1261–1267.
2. Khadra K, Parneix S, Angot P, Caltagirone J-P. Fictitious domain approach for numerical modelling of Navier–Stokes equations. *International Journal for Numerical Methods in Fluids* 2000; **34**:651–684.
3. Peyret R, Taylor TD. *Computational Methods for Fluid Flow*. Springer: New York, 1983.
4. Girault V, Raviart P-A. *Finite Element Methods for Navier–Stokes Equations*. Springer Series in Computational Mathematics. Springer: New York, 1986.



DOI: 10.1002/fld

5. Fortin M, Glowinski R. Méthodes de Lagrangien Augmenté, Application à la résolution numérique de problèmes aux limites. *Collection Méthodes Mathématiques de l'Informatique*, Dunod, 1982.
6. Vincent S, Caltagirone J-P, Lubin P, Randrianarivelo TN. An adaptative augmented Lagrangian method for three-dimensional multimaterial flows. *Computers and Fluids* 2004; **33**:1273–1289.
7. Breil J, Caltagirone JP. Three dimensional computer simulation of mould filling with N fluids by VOF PLIC and projection methods. *ICCFD*, Kyoto, 10–14 July 2000.
8. Le Bot C, Vincent S, Arquis E. Impact and solidification of indium droplets on a dry substrate. *International Journal of Thermal Sciences* 2005; **44**:219–233.
9. Lubin P, Vincent S, Caltagirone JP, Abadie S. Fully three-dimensional direct numerical simulation of a plunging breaker. *Comptes Rendus - Mecanique* 2003; **331**(7):495–501.
10. Chorin AJ. A numerical method for solving incompressible viscous flow problems. *Journal of Computational Physics* 1967; **2**:12–26.
11. Chorin AJ. Numerical simulation of the Navier–Stokes equations. *Mathematics of Computation* 1968; **22**:745–762.
12. Gresho PM, Chan ST. On the theory of semi-implicit projection methods for viscous incompressible flow and its implementation via a finite element method that also introduces a nearly consistent mass matrix. Part I: Theory. Part II: Implementation. *International Journal for Numerical Methods in Fluids* 1990; **11**:587–620, 621–659.
13. Hugues S, Randriamampianina A. An improved projection scheme applied to pseudospectral methods for the incompressible Navier–Stokes equations. *International Journal for Numerical Methods in Fluids* 1998; **28**:501–521.
14. Goda K. A multistep technique with implicit difference schemes for calculating two- or three-dimensional cavity flows. *Journal of Computational Physics* 1978; **30**:76–95.
15. Timmermans LJP, Minev PD, Van de Vosse FN. An approximate projection scheme for incompressible flow using spectral elements. *International Journal for Numerical Methods in Fluids* 1996; **22**:673–688.
16. Patankar SV, Spalding D. A calculation procedure for heat mass and momentum transfer in three dimensional parabolic flows. *International Journal of Heat and Mass Transfer* 1972; **15**:1787–1806.
17. Patankar SV. *Numerical Heat Transfer and Fluid flow*. Hemisphere Publishing Corporation: New York, 1980.
18. Caltagirone JP, Breil J. Sur une méthode de projection vectorielle pour la résolution des équations de Navier–Stokes. *Comptes Rendus de l' Academie des Sciences*, *Paris*, *Serie IIb* 1999; **327**:1179–1184.
19. Harlow FH, Welsh JE. Numerical calculation of time dependent viscous incompressible flows. *The Physics of Fluids* 1965; **8**:2182–2189.
20. Amestoy PR, Duff IS, L'Excellent J-Y. Multifrontal parallel distributed symmetric and unsymmetric solvers. *Computer Methods in Applied Mechanics and Engineering* 2000; **184**:501–520.
21. Quarteroni A, Valli A. *Domain Decomposition Methods for Partial Differential Equations*. *Numerical Mathematics and Scientific Computation*. Oxford Science Publications: Oxford, 1999.
22. Lions PL. On the Schwarz alternating method III: a variant for nonoverlapping subdomains. *Third International Symposium on Domain Decomposition Methods for Partial Differential Equations*, Philadelphia, 1990.
23. Bernardi C, Maday Y, Patera AT. Domain decomposition by the mortar element method. In *Asymptotic and Numerical Methods for Partial Differential Equations with Critical Parameters*. Kaper HG, Garbey M (eds). NATO ASI Series C, vol. 384. Kluwer Academic Publishers: Dordrecht, 1993; 269–286.
24. Cai XC, Dryja M, Sarkis M. Overlapping nonmatching grid Mortar element methods for elliptic problems. *SIAM Journal on Numerical Analysis* 1999; **36**:581–606.
25. Achdou Y, Maday Y, Widlund OB. Iterative substructuring preconditioners for mortar element methods in two dimensions. *SIAM Journal on Numerical Analysis* 1999; **36**(2):551–580.
26. Achdou Y, Japhet C, Maday Y, Nataf F. A new cement to glue non-conforming grids with Robin interface conditions: the finite volume case. *Numerische Mathematik* 2002; **92**(4):593–620.
27. Arbogast T, Yotov I. A non-mortar mixed finite element method for elliptic problems on non-matching multiblock grids. *Computer Methods in Applied Mechanics and Engineering* 1997; **149**(1–4):255–265.
28. Benek JA, Buning PG, Steger JL. A 3-D Chimera grid embedding technique. *AIAA 85-1523CP*, 1985.
29. Steger JL, Benek JA. On the use of composite grid schemes in computational aerodynamics. *Computer Methods in Applied Mechanics and Engineering* 1987; **64**:301–320.
30. Houzeaux G, Codina R. A Chimera method based on a Dirichlet/Neumann (Robin) coupling for the Navier–Stokes equations. *Computer Methods in Applied Mechanics and Engineering* 2003; **192**:3343–3377.
31. Brezzi F, Lions JL, Pironneau O. Analysis of a Chimera method. *Comptes Rendus de l' Academie des Sciences*, *Paris*, *Série I* 2001; **332**(I):655–660.



DOI: 10.1002/fld

32. Cadafalch J, Oliva A, Pérez-Segarra CD, Costa M, Salom J. Comparative study of conservative and nonconservative interpolation schemes for the domain decomposition method on laminar incompressible flow. *Numerical Heat Transfer*, *Part B* 1999; **35**:65–84.
33. Henshaw WD, Watson TJ. A fourth-order accurate method for the incompressible Navier–Stokes equations on overlapping grids. *Journal of Computational Physics* 1994; **113**(1):13–25.
34. Meakin RL. On the spatial and temporal accuracy of overset grid methods for moving body problems. *AIAA Applied Aerodynamics Conference*, 12th, Colorado Springs, CO, 20–22 June 1994, *Technical Papers*, Pt. 2 (A94-30939 10-02), American Institute of Aeronautics and Astronautics, Washington, DC, 1994; 858–871.
35. Burggraf OR. Analytical and numerical studies of the structure of the steady separated flow. *Journal of Fluid Mechanics* 1966; **24**:113–151.
36. Botella O, Peyret R. Benchmark spectral results on the lid-driven cavity flow. *Computers and Fluids* 1998; **4**:421–433.
37. Ghia U, Ghia KN, Shin CT. High-resolutions for incompressible flow using the Navier–Stokes equations and a multi-grid method. *Journal of Computational Physics* 1982; **48**:387–411.
38. Schreiber R, Keller HB. Driven cavity flow by efficient numerical techniques. *Journal of Computational Physics* 1983; **49**:310–333.
39. Bruneau CH, Jouron C. An efficient scheme for solving steady incompressible Navier–Stokes equations. *Journal of Computational Physics* 1990; **89**:389–413.
40. Barragy E, Carey GF. Stream function–vorticity driven cavity solution using p finite elements. *Computers and Fluids* 1997; **26**:453–468.
41. Armaly PH, Durst F, Pereira JCF, Schonung F. Experimental and theoretical investigation of backward-facing step flow. *Journal of Fluid Mechanics* 1983; **127**:473–496.
42. Lee T, Matescu D. Experimental and numerical investigation of 2-D backward-facing step flow. *Journal of Fluids and Structures* 1988; **12**:703–717.
43. Kim J, Moin P. Application of a fractional-step method to incompressible Navier–Stokes equations. *Journal of Computational Physics* 1985; **59**:308–323.
44. Barton IE. A numerical study of flow over a confined backward-facing step. *International Journal for Numerical Methods in Fluids* 1995; **21**:653–665.
45. Williams PT, Baker AJ. Numerical simulations of laminar flow over a 3D backward-facing step. *International Journal for Numerical Methods in Fluids* 1997; **24**:1159–1183.
46. Gartling DK. A test problem for outflow boundary conditions—flow over a backward-facing step. *International Journal for Numerical Methods in Fluids* 1990; **11**:953–967.
47. Sohn J. Evaluation of FIDAP on some classical laminar and turbulent benchmarks. *International Journal for Numerical Methods in Fluids* 1988; **8**:1469–1490.
48. Taneda S. Experimental investigation of the wakes behind cylinder at low Reynolds numbers. *Journal of the Physical Society of Japan* 1956; **11**:302–306.
49. Tritton DJ. Experiments on the flow past a circular cylinder at low Reynolds numbers. *Journal of Fluid Mechanics* 1959; **6**:547–567.
50. Acrivos A, Leal LG, Snowden DD, Pan F. Further experiments on steady separated flows past bluff objects. *Journal of Fluid Mechanics* 1968; **34**:25–48.
51. Coutanceau M, Bouard R. Experimental determination of the main features of the viscous flow in the wake of a circular cylinder in uniform translation. Part 1. Steady flow. *Journal of Fluid Mechanics* 1977; **79**:231–256.
52. Dennis SCR, Chang GZ. Numerical solutions for steady viscous flow past a circular cylinder. *Journal of Fluid Mechanics* 1970; **42**:471–489.
53. Nieuwstadt F, Keller HB. Viscous flow past circular cylinders. *Computer and Fluids* 1973; **1**:59.
54. Fornberg B. A numerical study of steady viscous flow past a circular cylinder. *Journal of Fluid Mechanics* 1980; **98**:819–855.
55. He X, Doolen G. Lattice Boltzman method on curvilinear coordinates system: flow around a circular cylinder. *Journal of Computational Physics* 1997; **134**:306–315.
56. Williamson CHK, Brown GL. A series in $1/\sqrt{Re}$ to represent the Strouhal–Reynolds number relationship of the cylinder wake. *Journal of Fluids and Structures* 1998; **12**:1073–1085.
57. Prabhakar V, Reddy JN. Spectral/hp penalty least-squares finite element formulation for the steady incompressible Navier–Stokes equations. *Journal of Computational Physics* 2006; **215**(1):274–297.



DOI: 10.1002/fld